



Effect of traverse speed on microstructure and mechanical properties of friction-stir-welded third-generation Al–Li alloy

Sanjeev Kumar¹ · Uttam Acharya¹ · Durjyodhan Sethi¹ · Tanmoy Medhi¹ · Barnik Saha Roy¹ · Subhash Chandra Saha¹

Received: 6 December 2019 / Accepted: 16 July 2020 / Published online: 22 July 2020
© The Brazilian Society of Mechanical Sciences and Engineering 2020

Abstract

The aim of the study is to investigate the consequences of tool traverse speed on force and torque distribution of friction-stir-welded third-generation Al–Cu–Li alloy joints. The microstructure and corresponding mechanical properties of the joints are investigated on force and torque perspective. Thus, the contribution of the present work lies in establishing the relation between traverse speed and mechanical properties of the AA2050-T84 joint. Four welds have been considered at varying traverse speeds from 1 to 4 mm/s at constant tool rotational speed and tool tilt angle of 1400 rpm and 2°, respectively. A tool of H13 steel having a tapered screw-threaded pin profile was used. The investigation reveals that with the increase in traverse speed, longitudinal force (*X*-force), vertically downward force (*Z*-force) and spindle torque also increase. The grain size of the nugget zone reduces from 19.84 to 14.86 μm as traverse speed increases. It has been found that the mechanical strength of the joint increases as the traverse speed increases. The Vickers microhardness value increases from 115 HV_{0.1} to 131 HV_{0.1} in the nugget zone as traverse speed increases from 1 to 4 mm/s. The maximum tensile strength, % elongation and joint efficiency are 403.2 MPa, 7.2% and 75.5% for traverse speed of 4 mm/s. The tensile fracture samples are analyzed by scanning electron microscope and reveal ductile mode of fracture.

Keywords AA2050 alloy · Friction stir welding · Traverse speed · Microstructure · Tensile strength · Microhardness · Fracture analysis

1 Introduction

The third-generation Al–Cu–Li alloy, namely AA2050-T84 (heat-treated) alloy, shows remarkable properties over other aluminum alloys, with a significant impetus to aerospace industry (lower and upper wing cover, spars, ribs, fuselage, empennage, cryogenic tank and internal structures) [1, 2]. AA2050-T84 alloy has excellent properties as compared to other Al alloy, viz. low density, high mechanical strength, improved strength-to-weight ratio, higher damage tolerance property and excellent corrosion resistance, with low anisotropy [3, 4]. This notable enhancement is mainly due to the presence of Li in AA2050-T84 alloy which decreases the density of alloy by 3%, increases the modulus of elasticity by

6% and increases the fatigue crack growth resistance considerably [5, 6]. Fine particle of the most efficient strengthening precipitate T1 (Al₂CuLi) phase was observed in high density which yielded higher strength per volume fraction [7]. Other intermetallic strengthening precipitates, for example θ'(Al₂Cu), δ'(Al₃Li), T2 (Al₅Li₃Cu), TB (Al₇Cu₄Li), can be observed in a lesser amount in Al–Cu–Li alloys [8]. However, the presence of intermediate Li content (< 1.4–1.5) in AA 2050 alloy limits the evolution of δ'(Al₃Li) precipitate, which reduces the fracture toughness [9, 10].

AA2xxx alloy when welded using conventional methods generates various defects including oxide layer, distortion, solidification cracking, porosity, etc. [11–14]. However, voids, tunnel, pinhole, wormhole, kissing bond, lack of penetration and joint-line remnant types of the defects are found in FSW joints due to improper material flow, insufficient consolidation of plasticized material and selection of inadequacy process parameter in FSW [15–19]. Further, these defects may be sorted out by the selection of optimum process parameters, tool and tool geometry which has reduced the chances of the defect in the weld. Friction stir welding

Technical Editor: Izabel Fernanda Machado, Dr.

✉ Sanjeev Kumar
placid.san@gmail.com

¹ National Institute of Technology Agartala, Barjala, Jirania, Tripura 799046, India

(FSW) can serve the purpose more efficiently as it joins the material in solid-state conditions. FSW is a variant of the green manufacturing process used to join ferrous, nonferrous, polymers, composite materials. The weld joint properties in FSW depend on various process parameters such as tool rotational speed (TRS), tool traverse speed (TTS), axial force, tool tilt angle (TTA), tool plunge depth, tool material and design, type of material to be joined and joint configuration, etc. Out of several parameters of FSW, TTS plays the key role and is one of the most important parameters as per the industrial point of view and improves the productivity of FSW. It has been reported that efficiency-wise TTS imparts 35% attention to the mechanical strength of the joint [20]. The TTS influences the extent of specific heat input generated during welding to achieve the sound and smooth joint in FSW [21]. Ideally, with an increase in TTS, the heat input decreases. Barenji [22] observed higher ultimate tensile strength (UTS) and hardness of welded AA7020 joint at higher TTS and ductile nature at higher heat input (lower TTS). Sakthivel et al. [23] studied the effect of increasing TTS (50–175 mm/min) on the mechanical properties of Al alloy joint. Results revealed that UTS, % elongation and grain size of NZ decrease with increase in TTS. Ni et al. [24] have also found a similar observation within a range of 300–1200 mm/min on 0.5-mm-thick AA 7075-T6 sheet. Liu et al. [25] introduced a self-reacting FSW tool to weld 4-mm-thick AA-6061-T6 sheet with varying TTS from 50 to 200 mm/min at constant TRS (600 rpm) to investigate the microstructure and mechanical properties in FSW. They observed defect-free joint was obtained at low TTS, while the UTS increases with increase in TTS value. Similarly, various researchers have studied the effect of TTS on different materials time-to-time. The above discussion suggests the importance of study based on TTS on a novel material like AA2050-T84, which lacks this type of analysis.

On the other hand, the force and torque evolved during welding also play a vital role that define the characteristics of welding in FSW. Some relevant studies in this field were reported by several researchers to show the effect of force and torque on the weldment as mentioned below. Lambiase et al. [16] welded 3-mm-thick AA6082-T6 alloy sheet at varying TTS (14.5, 21 & 31 mm/s) and observed that force and torque required to deform the material increase with an increase in TTS. Banik et al. [26] reported the effect of different tools and TTS on microstructure and mechanical property of 6-mm-thick AA6061-T6 plate in terms of forces & torque. It has been concluded from the study that torque and forces increase with an increase in TTS and accomplish superior value by taper threaded tool with low fluctuations. Acharya et al. [27] revealed the effect of torque and force on particle size in microstructure and mechanical properties of AA6092/17.5 SiCp-T6 MMC joint at varying TRS. It has been observed that the size of the reinforcement particles in

weldment is affected mainly by force and torque involved in the welding. The literature suggests that the quality and property of welding are primarily influenced by the force and torque evolved during welding. It also shows that the TTS also affects the extent of force and torque generated during welding.

The above discussions indicate the importance of a study carried out on TRS and force and torque evolved during welding. AA2050-T84 itself being a novel and high-strength alloy finds advanced applications but this lacks study. As per the best knowledge of the author, there is no such study reported till date, and this motivates the authors to carry out a work to uncover the effect of TTS on the force and torque evolution and its impact on overall microstructure and mechanical property of AA2050-T84 joint. In this study, a 5-mm-thick plate was FSWed using taper threaded tool at different TTSs and constant TRS. After that, the force and torque were evaluated in terms of variation in TTS through analysis microstructure and corresponding mechanical properties.

2 Experimental procedure

Dedicated 3T FSW welds AA2050-T84 plate with a dimension of 150 mm × 60 mm × 5 mm in square butt configuration with different TTSs of 1, 2, 3 and 4 mm/s at the constant TRS of 1400 rpm and TTA of 1.5°, respectively. The specification of 3T FSW is given in Table 1. The chemical composition and mechanical property of the base material (BM) are given in Table 2. A nonconsumable left-hand threaded tool of H13 tool steel as shown in Fig. 1 was rotated in an anticlockwise direction to perform the welding. When the tool rotates in anticlockwise direction, it presses the material inside the butt joint line along the direction of rotation with a downward movement and the required amount of heat generated softens the material which flew inward and provided higher strength to the joints. The details of the tool dimensions are given in Table 3. Before welding, the plates were cleaned by acetone to remove the dirt and foreign particle and rigidly fixed on machine bed for welding in parallel with the rolling direction. For each parameter, three sets of welding were performed to check the consistency in the welding condition. X-force, Z-force and spindle torque data which were generated during welding come from the data acquisition system (DAS) [LTC1090, eight channels of data with four isolated lines, manufactured by maxim integrated] and were used for analyzing the effect of these parameters on properties of welded material. DAS is a collection of software and hardware that allows to measure or control the physical parameters and obtains desirable results. It comprises mainly three elements (sensors, signal

Table 1 Specification of 3T FSW

Machine	3T friction stir welding unit
Machine no.	WS005
Stir welding operations	Linear welding
Welding options	Constant load/constant position on Z-axis
Spindle speed	3000 rpm max.–infinitely variable
Spindle torque-rated	86.4 Nm @ 1650 rpm
Tool force (axial load on spindle)	30 KN
Spindle tilting	$\pm 10^\circ$
Height of table from floor level	900 mm
Table clamping area	400 mm \times 275 mm
Axis travel	
X-axis	400 mm
Y-axis	50 mm
Z-axis (spindle slide)	100 mm
Feed rate	
X-axis	1000 mm/min. max.
Z-axis	30 KN max.
Thrust feedback	Through load cell
Axis movement	
X-axis	Servo motor—3000 rpm, 5Nm
Y-axis	Manual hydraulic cylinder
Z-axis drive	Servo hydraulic cylinder
Hydraulics	
Hydraulics tank capacity	110 L

Table 2 Chemical composition and mechanical property of AA2050 alloy

Chemical composition (weight %)										Mechanical properties		
Cu	Li	Ag	Mg	Mn	Zn	Zr	Ti	Fe	Si	UTS(MPa)	YS(MPa)	%EI
3.6	0.98	0.48	0.38	0.32	0.12	0.08	0.03	0.03	0.02	534.1	452.1	14.16

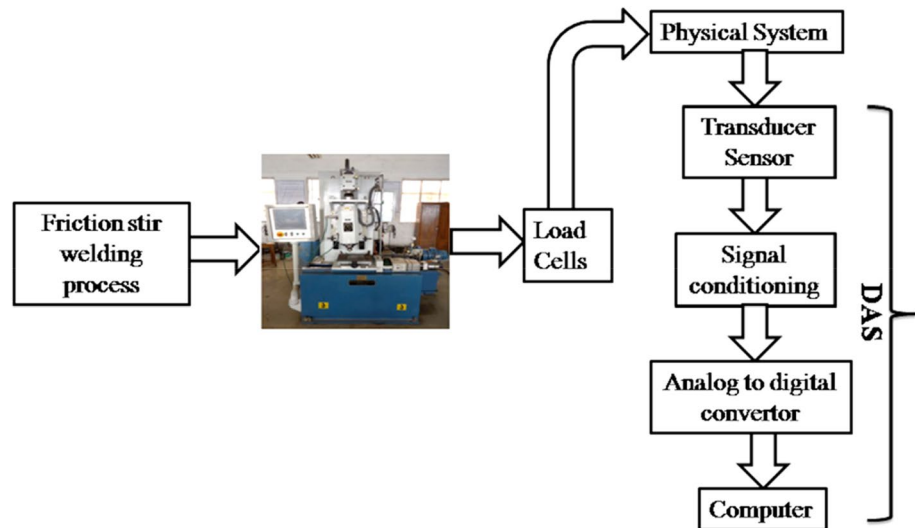
**Fig. 1** Friction stir tool used for the experiment

conditioning and analog-to-digital converter) where data generation and acquisition take place. Various types of data (*X*-force, *Z*-force, torque, etc.) generated by machine were gathered in physical system and fed (noisy electrical signals) to sensors, optimized (filtered and amplified signal) by signal conditioning to convert these signals into digital signals through analog-to-digital converter and finally displayed on monitor with the help of Rexroth programmable logic controller (PLC, integrated with IPC and NI LabVIEW software). The working configuration of DAS is elaborated in Fig. 2. This software is used for data acquisition, storage and retrieval purpose.

The heat input per unit length was obtained from the relation between the TRS, TTS and average torque. It affects the stirring action of the tool, softens the material and distributes the grain in stir zone according to the heat

Table 3 Tool dimensions used for friction stir welding

Shoulder diameter (mm)	Shoulder type	Concavity of shoulder	Pin type	Pin diameter (mm)		Pin length (mm)
				Tip diameter	Root diameter	
18	Concave	5°	Threaded	3	5	4.8

Fig. 2 Block diagram of process and data acquisition system

availability. For the preparation of samples (microstructure, hardness and tensile), the welded material is sliced out perpendicularly to the traverse direction of the joint from the position where the torque essentially remains constant during welding. The welded samples were polished using emery papers (grit size varying from 200 to 3000) followed by selvyt cloth polishing with hifin fluid, and different grades of diamond paste (1, 0.5 and 0.25 micron) were used for final polishing. Then, the samples were etched by modified Keller's reagent (3 ml HF, 6 ml HCl, 2 ml HNO₃ and 89 ml H₂O) to observe the characteristics of the microstructure and analysis of grain size of weld nugget zone under the microscope (light optical microscope, Leica DM2500). The diameter of the average grain size at the middle of the nugget zone was measured by the line intercept method according to ASTM E112-12 on Image-J software. Vickers hardness testing machine (Matsuzawa MMT-X Series) was employed for measuring the hardness across the thickness of joint in traverse direction of the weld as per ASTM E384-11e1 for all the samples. The hardness was measured in three different lines, viz. upper line (1 mm below the top surface), middle line (mid-thickness of the plate) and lower line (1 mm above the lower surface). Equal spacing of 1 mm was maintained between the two consecutive indentations by applying a load of 100 g for a dwell time of 10 s. For every experimental condition, to minimize the testing error, triplicate tensile samples were prepared according to ASTM

E8 and tested on Instron-1195 (UTM of 100KN capacity) machine. Samples were tested at a strain rate of 0.5 mm/min, and the values of ultimate tensile strength (UTS), yield stress, % elongation and joint efficiency (the ratio of UTS of welded sample to the UTS of base metal) were observed. The origin software is used to analyze the data (hardness and tensile) of the welded sample. The fracture analysis of the tensile sample was done by scanning electron microscope (SEM) to observe the nature of the failure pattern.

3 Results and discussion

In this section, the first part shows the consequences of TTS on variation in force, torque and heat input generated in the system during different welding. The second part shows the variation in weld bead surface appearance, macrostructure and microstructure of the joint in accordance with force, torque and heat input generated in the system. To understand the overall effect on mechanical property, the effect of TRS has been evaluated by analysis and comparing the grain size distribution of the weld zone of different welding.

3.1 Torque and force analysis

During welding, the variation in X-force, Z-forces and spindle torque as the tool proceeds is shown in Fig. 3a-c.

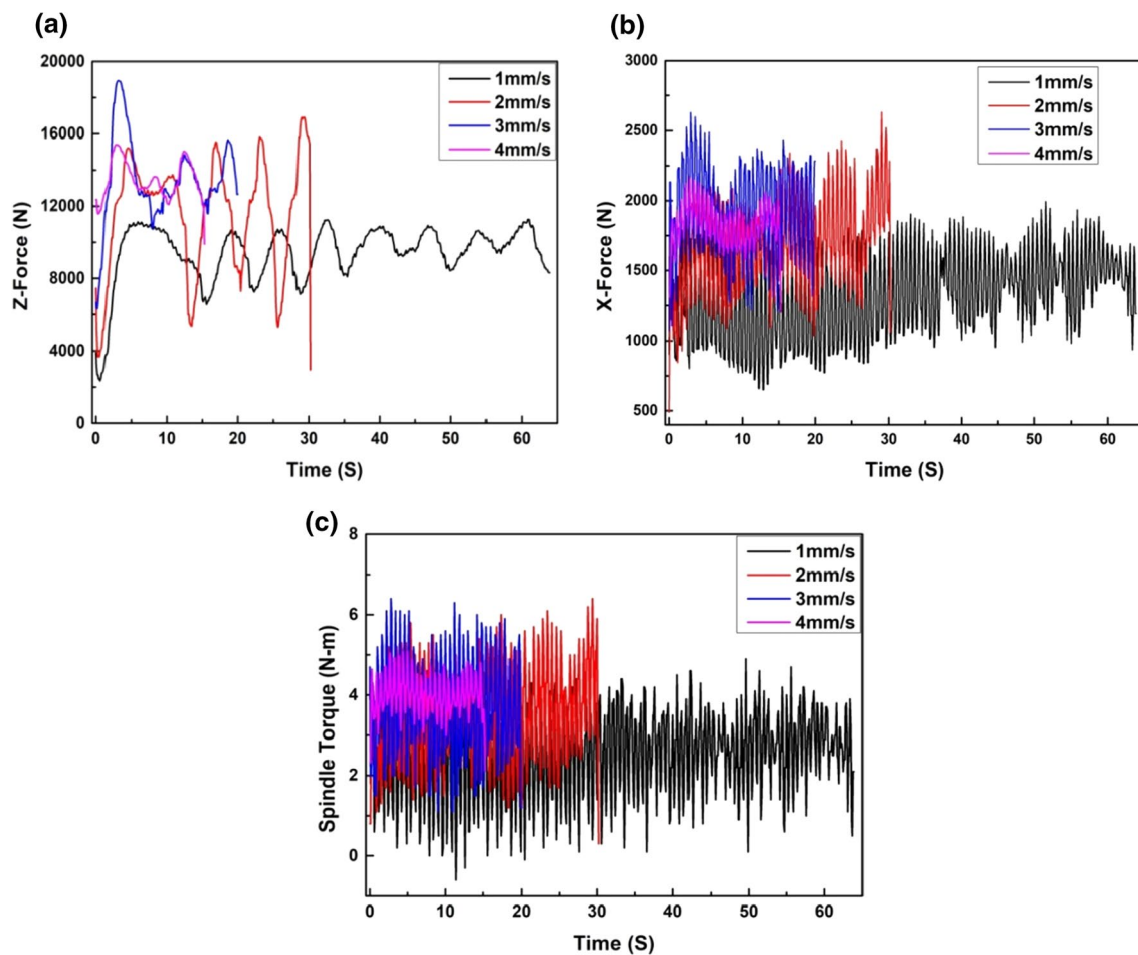


Fig. 3 Effect of tool traverse speed on **a** X-force, **b** Z-force and **c** spindle torque with respect to time

Here, it has to be noted that all the data for force and torque shown are exclusively measured during the actual weld run only and not during plunge time or dwell time. The forces (*X*-force, *Z* force) along with spindle torque were measured by strain gauge-based load cells which were obtained from DAS. The load cell attached with spindle head (5 tonnes) was used to measure spindle torque and *Z* force, whereas load cell attached with auxiliary slide (3 tonnes) was used to measure *X*-force. These load cells are controlled through a PLC (integrated with IPC and NI LabVIEW software), and the result is saved in storage device of computer. As the TTS increases from 1 to 3 mm/s, an abrupt variation in force and spindle torque distribution can be observed and thereafter it reduces for a TTS of 4 mm/s. Such variation in forces and torque may take place due to an uneven stick–slip phenomenon that may have stabilized at higher TTS.

Figure 4 shows the comparison of variation in the average value of forces and torque with the heat input at TTS. The variation in the average value of torque increases with increase in TTS. This is because as TTS increases, the requirement of force to deform the material will also

increase, and this increment in forces will lead to the requirement of the higher value of spindle torque to deform the material. It can be observed from the figure that with an increase in the TTS from 1 to 3 mm/s, the average value of *X* force and *Z* force increases. This observation is in agreement with the study made by Banik et al. [28]. However, in the case of *Z* force, it can be observed that the values do not increase with further increase in TTS from 3 to 4 mm/s. This suggests that the requirement of force to consolidate in its place is more as the TTS increases up to 3 mm/s. After this level of TTS, the state of the plasticized material may have attained such a value which may not require a higher amount of *Z*-force to consolidate the material. On the other hand, a similar observation can be made for *X*-force other than a decrease at the TTS of 4 mm/s. The decrease in the force exerted by material to the pin (*X*-force) indicates the ideal state of welding where it happens in a balanced mode of stick–slip phenomenon [27, 29, 30].

Further, the analysis of torque and force can also be supported by the amount of heat input involved in the welding. The heat input in the current work is calculated

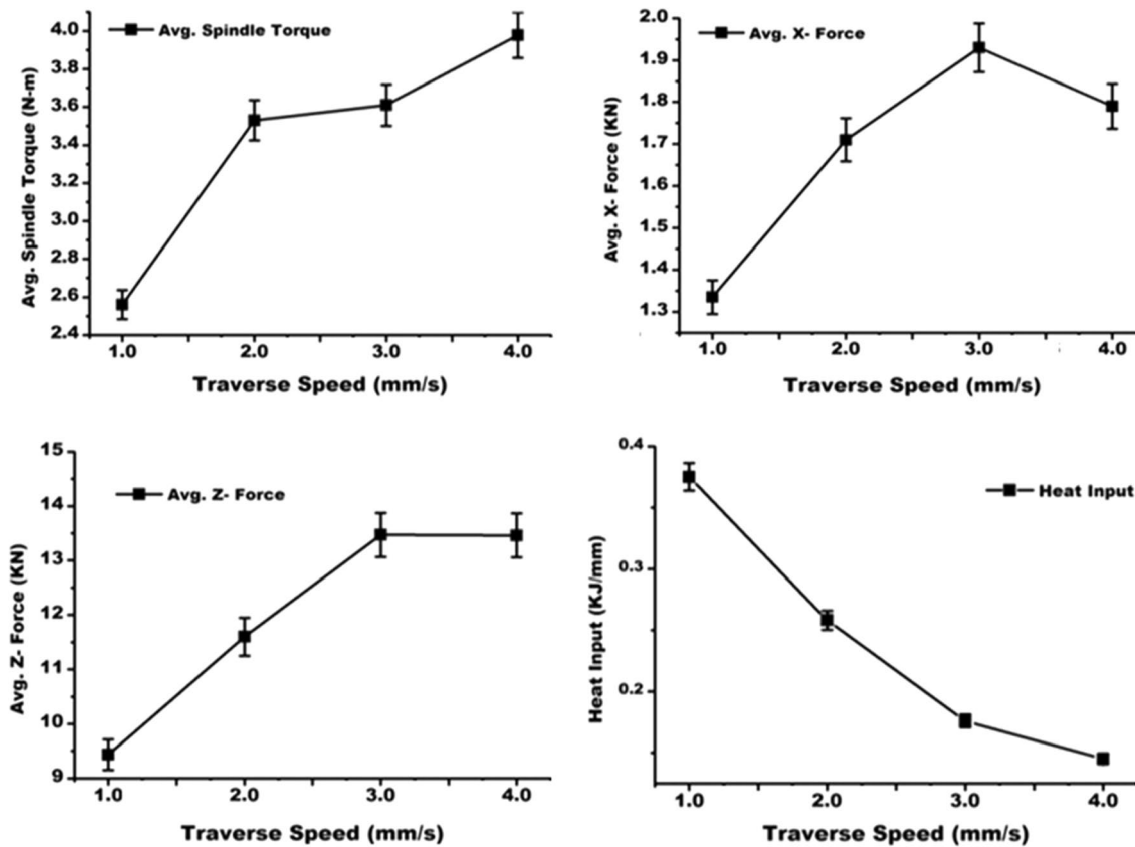


Fig. 4 Average X-force, Z-force and spindle torque with respect to varying traverse speeds

using Eq. (1), as shown below reported in [31, 32]. Here, each term contains notable meaning: for example, H is the heat input in J/mm, n is tool rotational speed in rotational per min, τ is the average torque in Nm and v is the TTS in mm/s. The average torque value is measured after the completion of dwelling phase which extends to the end phase of plunging out by the tool (during the FSW process). Although in transition period, torque is not stable, its incorporation does not affect the average value:


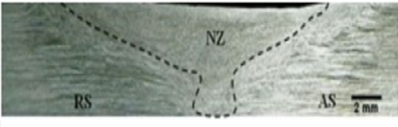

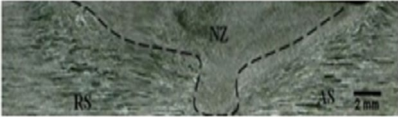



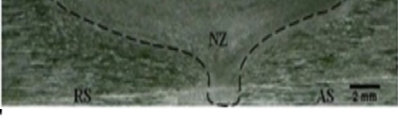
$$H = \frac{2\pi n\tau}{60V} \quad (1)$$

The figure shows a decreasing trend of heat input as the TTS increases. This is in line with the fact that as TTS increases, the tool–workpiece interaction time decreases, which facilitates lower friction heat to the process and results in a decrease in the overall heat input to the process. As the workpiece experiences less heat input with an increase in TTS, the force and torque required to deform the material also increase. It can also be seen that the difference in heat input for TTS of 3 mm/s and 4 mm/s is minimum as compared to others, which may result in such observations for X-force and Z-force.

3.2 Weld bead surface and macrostructure

Each welded sample was polished, and etching was done with modified Keller's reagent for 60–70 s carefully; then, it was washed with ethanol. This process is applicable for both macrostructure and microstructure. The weld bead appearance and respective macrostructure along the cross section for all sets of welding are presented in Table 4. All the friction-stir-welded samples were visually inspected and found defect-free, which was further observed under light optical microscope and analyzed by mechanical testing. The surface of the weld bead was found to be smooth, and absence of flash was seen. The absence of any defects indicates that all the welding has been conducted with the optimum level of the process parameter. A basin-shaped macrostructure was observed in the nugget zone. From the macrostructure, it can be observed that with increase in TTS, the area of the nugget zone decreases. This may be due to the low heat input generation; 70–80% of heat is generated through the interaction between the shoulder and workpiece during friction stir welding [33]. However, 2–20% of heat is generated from the plastic deformation and remaining heat from the interaction of the tool with the workpiece in weld [34]. The width of the weld zone increases at the shoulder interfacing surface area

Table 4 Weldment surface and microstructure of FSW joints produced at varying traverse speeds

Weld surface appearance	Macrostructure	Observation	Possible reason
		Defect-free joint	Proper flow of plasticized material
		Defect-free joint	Dynamic stirring action along with the adequate metal flow
		Defect-free joint	Adequate flow of plasticized metal
		Defect-free joint	sufficient flow of plasticized metal

due to high frictional heat and plastic deformation, whereas the heat extracted from underneath the tool pin area was found to be small [35].

3.3 Microstructural observation

The macroscopic observation shows different weld zones, viz. nugget zone (NZ), thermomechanically affected zone (TMAZ), heat-affected zone (HAZ) and base metal (BM). The microstructure of different zones shows variation in grain size and structure due to different heat inputs and flow of softened material at different TTSs. The microstructures of NZ and TMAZ in advance side (AS) and retreating side (RS) are observed under an optical microscope as shown in Fig. 5. The grain of NZ is more refined and equiaxed in shape as compared to other zones due to varied heat generation, which results in the nucleation and growth of new grain during plastic deformation. At the initial stage in NZ, the grains bend and get elongated. Further, the highly elongated grains break due to increase in the strain, and this process continues until equiaxed grain is formed [36]. The refinement of grain in TMAZ is mainly influenced by the shoulder friction during FSW where the elongated and tilted grain is formed from top to bottom of AS and RS in TMAZ which is elliptical in shape (as shown in Fig. 5.). This may be probably due to the nucleation of grain growth, which may be attributed by the generation of heat and shear force that tries to resist the material flow. On the other side, no such differentiation can be made between the grain of base material and HAZ, as they remain unaffected from thermal and mechanical effect [37, 38].

3.4 Grain size distribution

Figure 6 shows zonewise grain size distribution of the welded structures with varying TTSs which has been reported in the form of bar chart (with error). ImageJ software (having similar magnification, scale and most importantly possesses a similar area of $41,875 \mu\text{m}^2$) is used to measure grain size to standardize the study and for the sake of consistency of the result. The current section is being introduced in order to thoroughly understand the overall effect of TTS in the formation of the microstructure of the weld zone, which is ultimately responsible for the mechanical strength of the joint. The TTS will be evaluated in terms of force and torque and heat input in the joint. The study has been carried out by analyzing three optical microstructures (where grain is clearly observed) from each welding zone (NZ and TMAZ) as particular TTS is aimed to produce a result with minimum error. With increasing the TTS, the number of grain sizes has decreased due to the lower heat input, which affects the deformation rate during FSW. It can be observed from the figure that the highest grain size of NZ decreases from 36 to 33 μm as TTS increases from 1 to 4 mm/s, respectively. As far as the counts of smaller size grain (3–15 μm) are concerned, it also increases with an increase in TTS. The number of counts of grains in NZ is comparatively higher than the TMAZ (AS and RS) as the plasticised material of NZ sustains stirring action of the tool because of that there was a reduction in grain size (NZ). The rate of deformation and nucleation of grain is merely responsible for the heat generation and its distribution. The nucleation of

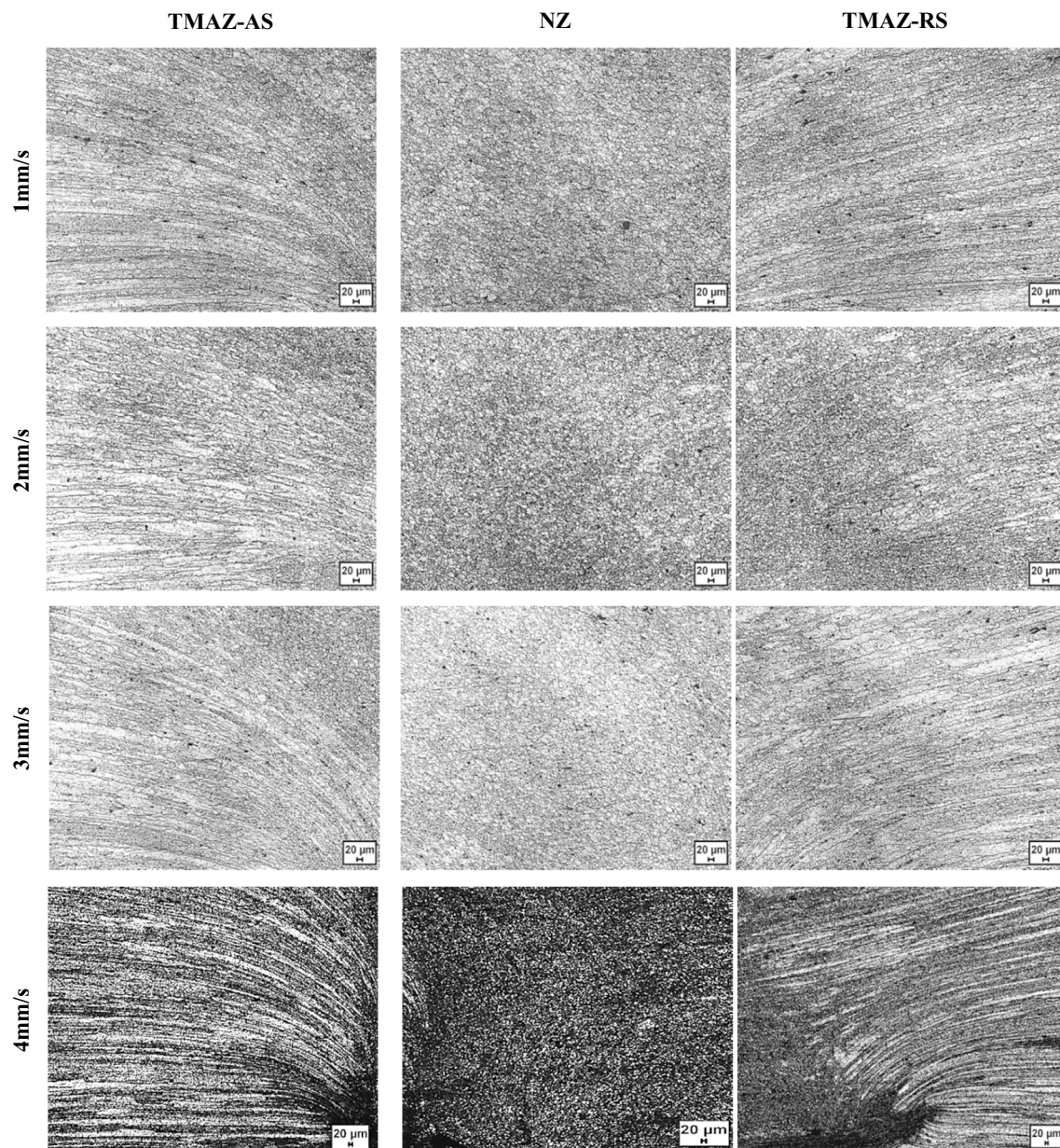


Fig. 5 Optical micrograph of the TMAZ-AS, NZ and TMAZ-RS at different tool traverse speeds

grain increases with increasing the temperature due to the straining effect. The growth rate of nucleation increases at lower TTS than the high, which facilitates the strain rate and the counts as an increase. The counts in TMAZ-RS is higher than the TMAZ-AS. It may be due to the flow of the plasticized material from AS to RS, which absorbs more heat to form the nucleation of grain growth. The nucleation of grain growth decreases due to less generation of heat at 4 mm/s, which affects the density of different elements and the grain size at the nugget zone. During high TTS, less amount of heat is generated, which affects the formation of the grain size.

Table 5 shows that with an increase in the TTS from 1 mm/s to 4 mm/s, average grain size of the NZ decreases from 19.84 to 14.86 μm. This may be due to the reduction in heat input per unit length. The same observation was reported by Sinhmar and Dwivedi and Evik et al. [39, 40]. At low TTS, the material of the workpiece and tool remains in contact for a comparatively longer time to provide higher temperature, which affects the formation of the grain size.

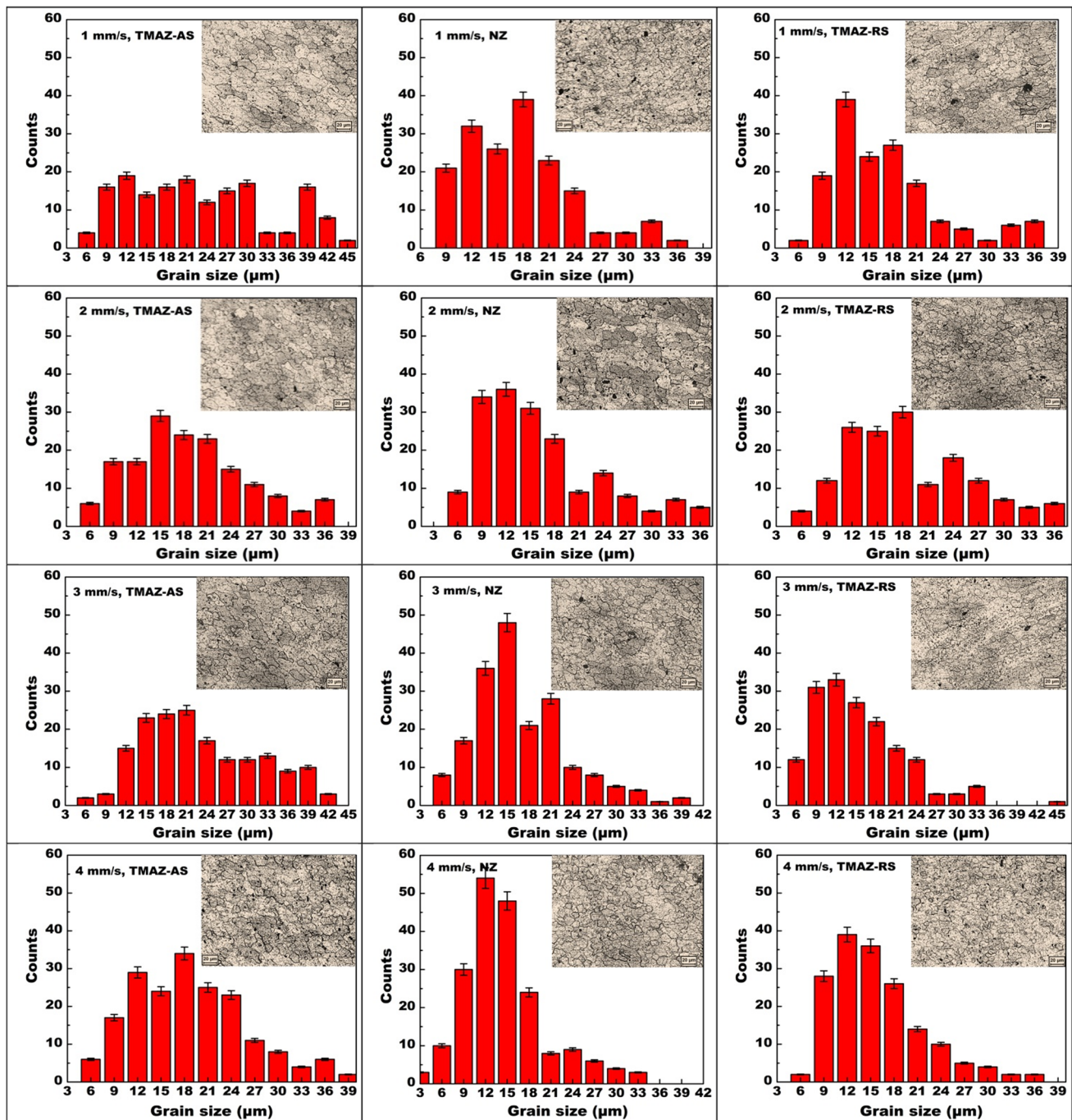


Fig. 6 Grain size distribution analysis of TMAZ-AS, NZ and TMAZ-RS for varying tool traverse speeds

Table 5 Average grain size of NZ at different tool traverse speeds

TTS	1 mm/s	2 mm/s	3 mm/s	4 mm/s
NZ	19.84 µm	17.10 µm	15.78 µm	14.86 µm

4 Mechanical property analysis

In this section, the overall effect of TTS on microstructural changes has been evaluated in terms of mechanical property changes of the joint, viz. microhardness (measured across the weld on traverse plane) and tensile strength of the joint. The fracture mode of the samples under tensile failure has also been observed.

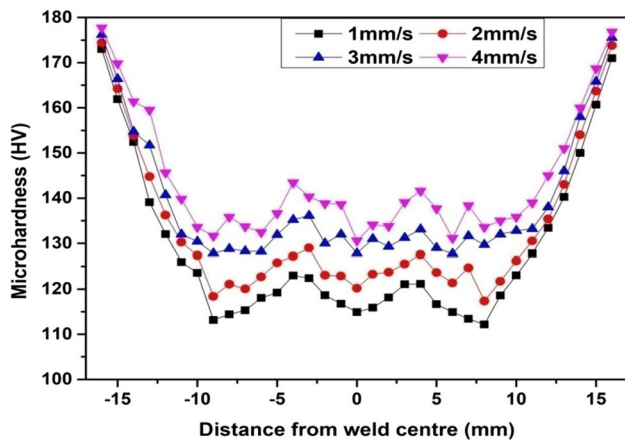


Fig. 7 Microhardness distribution profile of the joints at different traverse speeds

4.1 Hardness analysis

The hardness distribution profile across the thickness of the joint with varying TTS is shown in Fig. 7. However, for the simplicity of the study, the average hardness has been shown as all the three lines (top—1 mm below from the top surface, middle and lower—1 mm above from the lower surface) for a particular sample which are of the same characteristics as “W”-shaped hardness distribution profile. The average hardness of the base material is 175 HV_{0.1}. Hardness profile provides two pieces of crucial information—(1) the hardness of the base metal is higher than the welded material and (2) the lower TTS provides low hardness value of the joint because high heat is generated at low welding speed due to which large grain size is formed and according to Hall–Petch relation, grain size is inversely proportional to the hardness [41]. A similar observation was also seen in the present study according to which with increase in TTS (1–4 mm/s), the hardness of the NZ increases (115 HV_{0.1} to 131HV_{0.1}) along with a decrease in grain size (19.84–14.86 μm). The higher deformation and higher heat input lead to the dissolution of the second-phase precipitate, which results in the softening of the nugget zone and lower hardness in NZ. At different TTSS, NZ has a lower hardness value than the base metal. The hardness measured at HAZ is higher than the weld nugget due to the decrease in temperature, which affects the microstructure in this zone. The lowest hardness achieved in the RS at higher TTS is due to the less heat input and more force, torque and shearing action required for the flowability of the material on RS.

4.2 Effect of traverse speed on tensile strength

Figure 8 depicts the tensile strength (which was carried out by Instron-1195) of welded AA2050-T84 alloy joints at

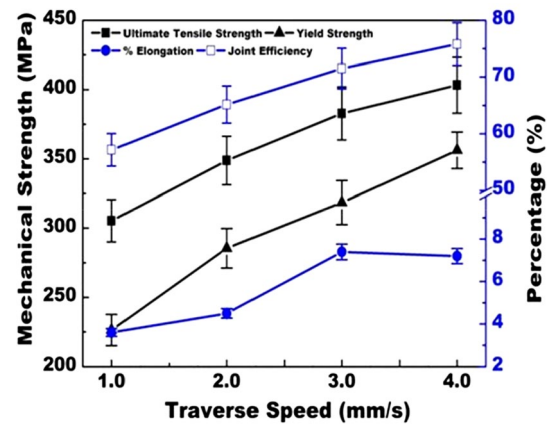


Fig. 8 Tensile properties of the welded sample at different traverse speeds

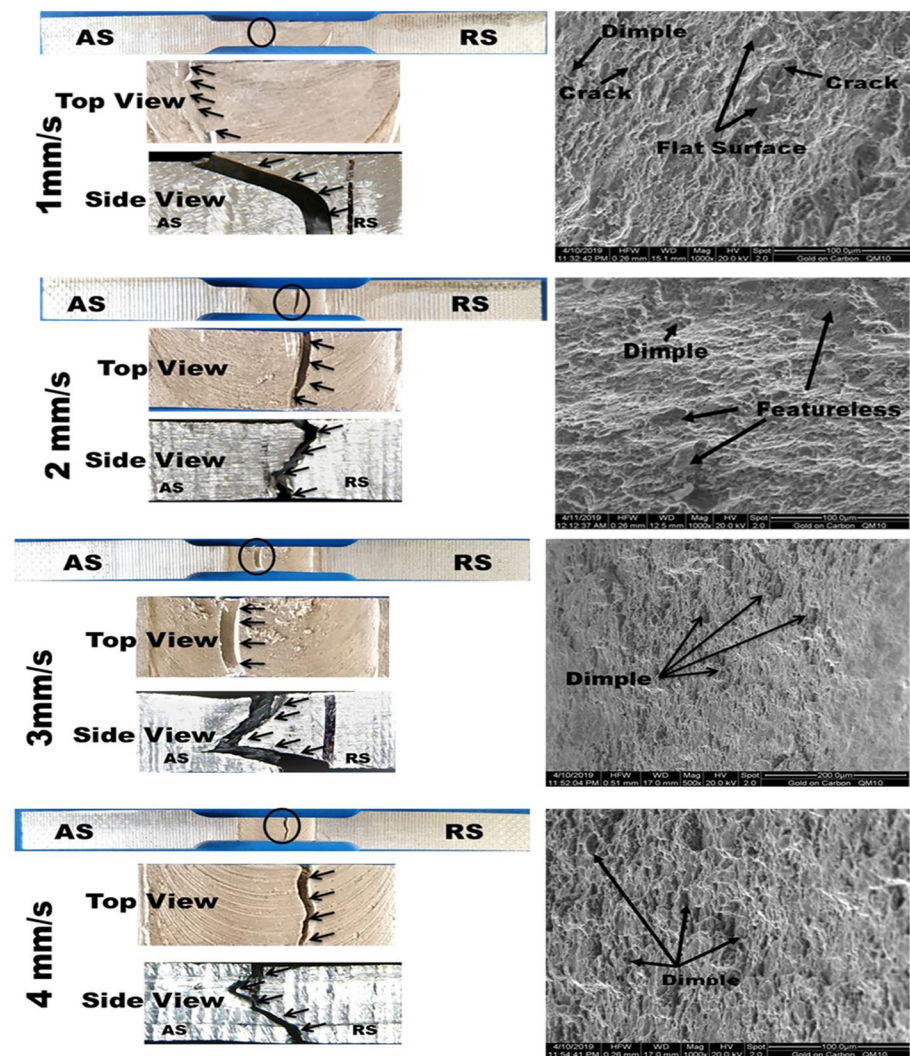
different TTSS and constant TRS of 1400 rpm. The figure shows that as TTS increases from 1 mm/s to 4 mm/s, the ultimate tensile strength (UTS), yield stress (YS), % elongation and joint efficiency (the ratio of the ultimate tensile strength of joints to the ultimate tensile strength of the base material) of the joint also increase. However, all the entities of the strength (UTS, YS and % elongation) of the welded joint were observed to be lower than those of the base material. The maximum tensile strength, % elongation and % joint efficiency achieved at 4 mm/s are 403.2 MPa, 7.2 and 75.5, respectively. However, the lower tensile properties are observed at 1 mm/s. Such an increase in trend with an increase in TTS may be due to the direct effect of heat input on the grain size distribution of the welded structure. The heat input influences the effect of TTS on the tensile properties of the welded sample. With increasing TTS, generation of heat input decreases; as a result, the grain growth at lower heat input is restricted and comparatively smaller in size. The relation between grain size and yield strength is described mathematically by Hall–Petch equation, which is shown in Eq. (2), where “ σ_y ” denotes the yield stress, “ σ_0 ” friction stress in the absence of grain boundaries, “ k ” strengthening coefficient and “ D ” average grain size diameter [42, 43]. As per the Hall–Petch equation, the smaller the grain size, the higher the strength. A similar trend was observed while the experiment was performed.

$$\sigma_y = \sigma_0 + \frac{k}{\sqrt{D}} \quad (2)$$

4.2.1 Fractographic analysis

Figure 9 represents the fractographic analysis of fractured tensile samples for different TTSS. For the sake of easy understanding, the close view (top view and side view) of

Fig. 9 Fractured tensile specimen with top view, side view and higher magnified SEM image of the fracture surface



the fractured tensile samples is also presented in the figure. The fractured tensile sample is studied by SEM to reveal the nature of the failure. It is observed from the figure that the fracture initiated from the weld surface and gradually propagated through a particular path in the material to complete the fracture. A line is drawn on the center position of the welded region before tensile testing was done as shown on the side view in Fig. 9 to ensure the side of the fracture. It can be observed that the fracture of the welded joint initiated from the NZ with all TTSs except 3 mm/s. The fracture location of the tensile specimen at 3 mm/s has taken place at HAZ on AS of the welded joint. The higher heat generated at lower TTS (1 mm/s) produces flat surfaces with cracks, which reduces the strength. With increasing TTS from 1 to 2 mm/s, a featureless pattern without any crack was observed in SEM image. Further, with increase in TTS (3 mm/s), a cone-type fracture was observed in a broken tensile sample, which indicates the ductile nature of the welded joint. The population of dimple increases at high TTS (4 mm/s),

which indicates the ductile mode of failure (observed from the fractography) and provides maximum tensile strength due to adequate heat generation during welding.

5 Conclusions

In this study, 5-mm-thick AA2050-T84 plates have been successfully welded at different TTSs by keeping the other parameters constant through FSW. The variation in force and torque was studied as a function of variation in TTS, and the microstructure and mechanical properties of the joint are studied. The outcomes of the study are concluded below:

- The study reveals that X-force and Z-force increase (from 1327.58 to 1943.12 N and 9435.27 to 13476.37 N), respectively, with increase in TTS from 1 to 3 mm/s and then decrease (1817.39 and 13464.71 N) with further increase in TTS to 4 mm/s. However, spindle torque

increases from 2.56 to 3.98 Nm with increase in TTS from 1 to 3 mm/s. The heat input decreases from 0.58 to 0.14 kJ/mm as TTS increases from 1 to 4 mm/s.

- The defect-free joint was produced on AA 2050-T84 alloy at various TTSs (1–4 mm/s) at constant TRS through friction stir welding. With increase in TTS, the flashing problem has been reduced and sound weld bead appearance has been observed.
- The elongated grains were observed at the TMAZ due to less deformation of material, and equiaxed grains were observed in the NZ due to increased heat generation. The average grain size in the nugget zone decreases with increase in TTS from 19.84 to 14.86 μm .
- The hardness of the nugget zone increases from 115 HV_{0.1} to 131HV_{0.1} with increased TTS from 1 to 4 mm/s. The maximum tensile strength of 403.2 MPa was observed at 4 mm/s, which is 32% more from the lower tensile strength (1 mm/s). The maximum weld efficiency of 75.5% has been reported at TTS of 4 mm/s. The tensile fractured sample shows the ductile mode of failure.

Acknowledgements The authors would like to sincerely acknowledge the funding support from MHRD to carry out the research work. The authors are grateful to the Department of Mechanical Engineering, IIT Kanpur, India, for extending the facilities of Material Testing Laboratory to perform the experiments.

References

1. Wanhill RJH, Bray GH (2014) Aerostructural design and its application to aluminum–lithium alloys. In: Eswara Prasad N, Gokhale AA, Wanhill R (eds) Aluminum–lithium alloys. Butterworth-Heinemann, Oxford, pp 27–58
2. Rioja RJ, Liu J (2012) The evolution of Al–Li base products for aerospace and space applications. *Metall Mater Trans A* 43(9):3325–3337. <https://doi.org/10.1007/s11661-012-1155-z>
3. Chu Q, Li WY, Hou HL, Yang XW, Vairis A, Wang C, Wang WB (2019) On the double-side probeless friction stir spot welding of AA2198 Al–Li alloy. *J Mater Sci Technol* 35(5):784–789. <https://doi.org/10.1016/j.jmst.2018.10.027>
4. El-Aty AA, Xu Y, Guo X, Zhang SH, Ma Y, Chen D (2018) Strengthening mechanisms, deformation behavior, and anisotropic mechanical properties of Al–Li alloys: a review. *J Adv Res* 10:49–67. <https://doi.org/10.1016/j.jare.2017.12.004>
5. Prasad NE, Gokhale A, Wanhill RJH (eds) (2013) Aluminum–lithium alloys: processing, properties, and applications. Butterworth-Heinemann, Oxford
6. Yan K, Wang T, Liang H, Zhao Y (2018) Effects of rotation speed on microstructure and mechanical properties of 2060 Al–Cu–Li alloy in friction stir welding. *J Mater Eng Perform* 27(11):5803–5814. <https://doi.org/10.1007/s11665-018-3650-x>
7. Niedzinski M (2019) The evolution of constellium Al–Li alloy for space launch and crew module application. *Light Met Age* 77:36–42
8. Avettand-Fènoël MN, De Geuser F, Deschamps A (2019) Effect of the ageing on precipitation spatial distribution in stationary shoulder friction stir welded AA2050 alloys. *Mater Charact* 154:193–199. <https://doi.org/10.1016/j.matchar.2019.06.006>
9. Sidhar H, Mishra RS, Reynolds AP, Baumann JA (2017) Impact of thermal management on post weld heat treatment efficacy in friction stir welded 2050-T3 alloy. *J Alloy Compd* 722:330–338. <https://doi.org/10.1016/j.jallcom.2017.06.141>
10. Lequeu P, Smith KP, Daniélou A (2010) Aluminum–copper–lithium alloy 2050 developed for medium to thick plate. *J Mater Eng Perform* 19(6):841–847. <https://doi.org/10.1007/s11665-009-9554-z>
11. Cisko AR, Jordon JB, Avery DZ, Liu T, Brewer LN, Allison PG, Carino RL, Hammi Y, Rushing TW, Garcia L (2019) Experiments and modeling of fatigue behavior of friction stir welded aluminum lithium alloy. *Metals* 9(3):293
12. Kah P, Rajan R, Martikainen J, Suoranta R (2015) Investigation of weld defects in friction-stir welding and fusion welding of aluminium alloys. *Int J Mech Mater Eng* 10(1):26. <https://doi.org/10.1186/s40712-015-0053-8>
13. Liu H, Hu Y, Dou C, Sekulic DP (2017) An effect of the rotation speed on microstructure and mechanical properties of the friction stir welded 2060-T8 Al–Li alloy. *Mater Charact* 123:9–19. <https://doi.org/10.1016/j.matchar.2016.11.011>
14. Moshwan R, Yusof F, Hassan MA, Rahmat SM (2015) Effect of tool rotational speed on force generation, microstructure and mechanical properties of friction stir welded Al–Mg–Cr–Mn (AA 5052-O) alloy. *Mater Des* 1980–2015(66):118–128. <https://doi.org/10.1016/j.matdes.2014.10.043>
15. Dialami N, Cervera M, Chiumenti M, Segatori A (2019) Prediction of joint line remnant defect in friction stir welding. *Int J Mech Sci* 151:61–69. <https://doi.org/10.1016/j.ijmecsci.2018.11.012>
16. Dehghani M, Amadeh A, Akbari Mousavi SAA (2013) Investigations on the effects of friction stir welding parameters on intermetallic and defect formation in joining aluminum alloy to mild steel. *Mater Des* 49:433–441. <https://doi.org/10.1016/j.matdes.20113.01.013>
17. Tarasov SY, Rubtsov VE, Eliseev AA, Kolubaev EA, Filippov AV, Ivanov AN (2015) Effect of friction stir welding parameters on defect formation, advanced materials with hierarchical structure for new technologies and reliable structure. *AIP Conf Proc* 1683:020230–1–020230-5. <https://doi.org/10.1063/1.4932920>
18. Brotherhood CJ, Drinkwater BW, Dixon S (2003) The detectability of kissing bonds in adhesive joints using ultrasonic techniques. *Ultrasonic* 41(7):521–529. [https://doi.org/10.1016/S0041-624X\(03\)00156-2](https://doi.org/10.1016/S0041-624X(03)00156-2)
19. Hu Y, Liu H, Li S, Du S, Sekulic DP (2018) Improving mechanical properties of a joint through tilt probe penetrating friction stir welding. *Mater Sci Eng A* 731(25):107–118. <https://doi.org/10.1016/j.msea.2018.06.036>
20. Panda B, Garg A, Jian Z, Heidarzadeh A, Gao L (2016) Characterization of the tensile properties of friction stir welded aluminum alloy joints based on axial force, traverse speed, and rotational speed. *Front Mech Eng* 11(3):289–298. <https://doi.org/10.1007/s11465-016-0393-y>
21. Lambiase F, Paoletti A, Di Ilio A (2018) Forces and temperature variation during friction stir welding of aluminum alloy AA6082-T6. *Int J Adv Manuf Technol* 99(1–4):337–346. <https://doi.org/10.1007/s00170-018-2524-6>
22. Barenji RV (2016) Effect of tool traverse speed on microstructure and mechanical performance of friction stir welded 7020 aluminum alloy. *Proc Inst Mech Eng Part L J Mater Des Appl* 230(2):663–673. <https://doi.org/10.1177/1464420715584950>
23. Sakthivel T, Sengar GS, Mukhopadhyay J (2009) Effect of welding speed on microstructure and mechanical properties of friction-stir-welded aluminum. *Int J Adv Manuf Technol* 43(5–6):468–473. <https://doi.org/10.1007/s00170-008-1727-7>

24. Ni Y, Fu L, Chen HY (2019) Effects of travel speed on mechanical properties of AA7075-T6 ultra-thin sheet joints fabricated by high rotational speed micro pinless friction stir welding. *J Mater Process Technol* 265:63–70. <https://doi.org/10.1016/j.jmatprotec.2018.10.006>
25. Liu HJ, Zhang HJ, Yu L (2011) Effect of welding speed on microstructures and mechanical properties of underwater friction stir welded 2219 aluminum alloy. *Mater Des* 32(3):1548–1553. <https://doi.org/10.1016/j.matdes.2010.09.032>
26. Banik A, Roy BS, Barma JD, Saha SC (2018) An experimental investigation of torque and force generation for varying tool tilt angles and their effects on microstructure and mechanical properties: Friction stir welding of AA 6061-T6. *J Manuf Process* 31:395–404. <https://doi.org/10.1016/j.jmapro.2017.11.030>
27. Acharya U, Roy BS, Saha SC (2019) Torque and force perspectives on particle size and its effect on mechanical property of friction stir welded AA6092/17.5 SiCp-T6 composite joints. *J Manuf Process* 38:113–121. <https://doi.org/10.1016/j.jmapro.2019.01.009>
28. Banik A, Barma JD, Saha SC (2019) Effect of threaded pin tool for friction stir welding of AA6061-T6 at varying traverse speeds: torque and force analysis. *Iran J Sci Technol Trans Mech Eng.* <https://doi.org/10.1007/s40997-019-00289-w>
29. Sharma N, Siddiquee AN, Khan ZA, Mohammed MT (2017) Material stirring during FSW of Al–Cu: effect of pin profile. *Mater Manuf Process.* <https://doi.org/10.1080/10426914.2017.138852>
30. Tiwari A, Pankaj P, Biswas P, Kore SD, Rao AG (2019) Tool performance evaluation of friction stir welded shipbuilding grade DH36 steel butt joints. *Int J Adv Manuf Technol.* <https://doi.org/10.1007/s00170-019-03618-0>
31. Medhi T, Yadava MK, Roy BS, Saha SC (2019) An experimental investigation on implications of traverse speed in joining of dissimilar Al–Cu by friction stir welding. *Int J Adv Manuf Technol* 104(1–4):1461–1471. <https://doi.org/10.1007/s00170-019-04086-2>
32. Ramanjaneyulu K, Madhusudhan Reddy GM, Rao AV (2014) Role of tool shoulder diameter in friction stir welding: an analysis of the temperature and plastic deformation of AA2014 aluminium alloy. *Trans Indian Inst Met.* <https://doi.org/10.1007/s12666-014-0401-z>
33. Hassan KA, Prangnell PB, Norman AF, Price DA, Williams SW (2003) Effect of welding parameters on nugget zone microstructure and properties in high strength aluminium alloy friction stir welds. *Sci Technol Weld Join* 8(4):257–268. <https://doi.org/10.1179/136217103225005480>
34. Chen Y, He C, Yang K, Zhang H, Wang C, Wang Q, Liu Y (2019) Effects of microstructural inhomogeneities and micro-defects on tensile and very high cycle fatigue behaviors of the friction stir welded ZK60 magnesium alloy joint. *Int J Fatigue* 122:218–227. <https://doi.org/10.1016/j.ijfatigue.2019.01.016>
35. Essa GM, Zakria HM, Mahmoud TS, Khalifa TA (2018) Microstructure examination and microhardness of friction stir welded joint of (AA7020-O) after PWHT. *HBRC J* 14(1):22–28. <https://doi.org/10.1016/j.hbrj.2015.05.002>
36. Zhou L, Li GH, Zha GD, Shu FY, Liu HJ, Feng JC (2018) Effect of rotation speed on microstructure and mechanical properties of bobbin tool friction stir welded AZ61 magnesium alloy. *Sci Technol Weld Join* 23(7):596–605. <https://doi.org/10.1080/13621718.2018.1432098>
37. Carlone P, Palazzo GS (2013) Influence of process parameters on microstructure and mechanical properties in AA2024-T3 friction stir welding. *Metallogr Microstruct Anal* 2(4):213–222. <https://doi.org/10.1007/s13632-013-0078-4>
38. Threadgill PL, Leonard AJ, Shercliff HR, Withers PJ (2009) Friction stir welding of aluminium alloys. *Int Mater Rev* 54(2):49–93. <https://doi.org/10.1179/174328009x411136>
39. Sinhmar S, Dwivedi DK (2019) Effect of weld thermal cycle on metallurgical and corrosion behavior of friction stir weld joint of AA2014 aluminium alloy. *J Manuf Process* 37:305–320. <https://doi.org/10.1016/j.jmapro.2018.12.001>
40. Cevik B, Ozcatalbas Y, Gülenç B (2016) Effect of welding speed on the mechanical properties and weld defects of 7075 Al alloy joined by FSW. *Kovove Mater* 54(4):241–247. https://doi.org/10.4149/km_2016_4_241
41. Izadi H, Sandstrom R, Gerlich AP (2014) Grain growth behavior and hall–petch strengthening in friction stir processed Al 5059. *Metall Mater Trans A* 45:5635. <https://doi.org/10.1007/s11661-014-2492-x>
42. Carlton CE, Ferreira PJ (2007) What is behind the inverse Hall–Petch effect in nanocrystalline materials? *Acta Mater* 55:3749–3756. <https://doi.org/10.1016/j.actamat.2007.02.021>
43. Cordero ZC, Knight BE, Schuh CA (2016) Six decades of the Hall–Petch effect—a survey of grain-size strengthening studies on pure metals. *Int Mater Rev* 61(8):495–512. <https://doi.org/10.1080/09506608.2016.1191808>

Publisher's Note Springer Nature remains neutral with regard to jurisdictional claims in published maps and institutional affiliations.